

Lateral transition metal dichalcogenide heterostructures for high efficiency thermoelectric devices

Sathwik Bharadwaj,^{1,2} Ashwin Ramasubramaniam,^{3,*} and L. R. Ram-Mohan^{1,2,†}

¹*Department of Physics, Worcester Polytechnic Institute, Worcester, Massachusetts 01609, USA.*

²*Center for Computational NanoScience, Worcester Polytechnic Institute, Worcester, Massachusetts 01609, USA.*

³*Department of Mechanical and Industrial Engineering, University of Massachusetts, Amherst, Massachusetts 01003, USA.*

Increasing demands for renewable sources of energy has been a major driving force for developing efficient thermoelectric materials. Two-dimensional (2D) transition-metal dichalcogenides (TMDC) have emerged as promising candidates for thermoelectric applications due to their large effective mass and low thermal conductivity. In this article, we study the thermoelectric performance of lateral TMDC heterostructures within a multiscale quantum transport framework. Both *n*-type and *p*-type lateral heterostructures are considered for all possible combinations of semiconducting TMDCs: MoS₂, MoSe₂, WS₂, and WSe₂. The band alignment between these materials is found to play a crucial role in enhancing the thermoelectric figure-of-merit (*ZT*) and power factor far beyond those of pristine TMDCs. In particular, we show that the room-temperature *ZT* value of *n*-type WS₂ with WSe₂ triangular inclusions, is five times larger than the pristine WS₂ monolayer. *p*-type MoSe₂ with WSe₂ inclusions is also shown to have a room-temperature *ZT* value about two times larger than the pristine MoSe₂ monolayer. The peak power factor values calculated here, are the highest reported amongst gapped 2D monolayers at room temperature. Hence, 2D lateral TMDC heterostructures open new avenues to develop ultra-efficient, planar thermoelectric devices.

Keywords: thermoelectricity, two-dimensional materials, transition-metal dichalcogenides, lateral heterostructures, planar devices

December 4, 2020

Thermoelectric devices can play a pivotal role in fulfilling future demands for clean energy [1–3]. A good thermoelectric material must have a high thermoelectric figure-of-merit *ZT*, defined as

$$ZT = \frac{\sigma S^2 T}{\kappa_e + \kappa_{ph}}, \quad (1)$$

where *T* is the absolute temperature, σ is the electrical conductance, *S* is the Seebeck coefficient, κ_e is the electronic thermal conductivity, and κ_{ph} is the lattice phonon thermal conductivity. In bulk materials, the *ZT* value is limited by σ and *S* varying in inverse proportion, and κ_e and σ varying in direct proportion (Wiedemann-Franz law) [4]. Hence, for a long period of time thermoelectricity was believed to be an inefficient source of energy for practical application [5]. However, works by Hicks and Dresselhaus [6–8] illustrated that in nanostructures, one could achieve a substantial increase in the value of *ZT* by reducing the dimensionality of the system. The density of electronic states per unit volume increases in lower dimensions, thereby resulting in an enhancement in *ZT* [9]. Since then the field of thermoelectricity has focused on: a) increasing *S* and σ independently through quantum confinement effects, and b) decreasing κ_{ph} by systematically controlling phonon contributions [10]. Additionally, other techniques such as band-gap engineering

[11], carrier-pocket engineering [12], energy filtering [13], and semimetal–semiconductor transition [14] have been developed to engineer the thermoelectric properties of nanostructures.

Traditionally, semiconductor superlattices and heterostructures have been used to construct efficient thermoelectric devices. However, in such structures, it is experimentally difficult to achieve the efficiency predicted by theory since a large number of parameters have to be optimized [15]. In this regard, two-dimensional (2D) materials such as graphene and transition-metal dichalcogenides (TMDC) have attracted tremendous attention due to their unique physical and chemical properties [16]. The high degree of flexibility of 2D materials to tune the electrical and thermal properties, makes them ideal candidates for thermoelectric applications. The prototypical 2D material, graphene, has exhibited a power factor (PF) value as high as 34.5 mWm⁻¹K⁻² at room temperature [17]. However, it has limited thermoelectric applications due to an extremely high thermal conductivity (2000 – 4000 Wm⁻¹K⁻¹ for freely suspended samples at room temperature [18, 19]). In comparison, monolayer (1L) TMDCs maintain a very low thermal conductance due to significantly lower phonon mean-free paths [20, 21]. Hence, TMDCs have tremendous potential to realize in-plane thermoelectric and Peltier cooling devices.

There have been several first-principles studies on calculating the thermoelectric quantities in 1L and layered TMDCs [22–27, 29]. *p*-type MoS₂ 1L and *n*-type WSe₂ 1L were observed to have maximum *ZT* values at room temperature and at higher temperatures, respectively. Also, bilayer MoS₂ was observed to have a PF of 8.5 mWm⁻¹K⁻², which is the highest amongst mate-

* ashwin@engin.umass.edu

† lrram@wpi.edu

rials with a non-zero bandgap [27]. Yet the conductance and ZT values observed in TMDCs are much lower than the corresponding quantities in traditional thermoelectric materials such as Bi_2Te_3 , and phonon-glass electron-crystals [28]. Thus, there are opportunities to boost the thermoelectric performance in TMDCs through the formation of heterostructures, as delineated in this article.

Similar crystal structure and comparable lattice constants of MX_2 ($M = \text{Mo}, \text{W}$; $X = \text{S}, \text{Se}$) monolayers have motivated the construction of lateral TMDC heterostructures. Experimentally, such structures are fabricated through multistep chemical vapor deposition techniques [30–34], one-pot synthesis [35], and omnidirectional epitaxy [36]. In traditional thermoelectric materials, such as Bi_2Te_3 , quantum confinement through the formation of heterostructures has been demonstrated to enhance the figure-of-merit [37, 38]. Thus, we may anticipate such an enhancement in lateral 2D TMDC heterostructures as well.

In this article, we study the thermoelectric performance of lateral TMDC heterostructures within a multiscale quantum transport framework with inputs from first-principles calculations. We specifically consider triangular inclusions (see Fig. 1), since 2D TMDCs are typically grown as triangular flakes. We study both n -type and p -type lateral heterostructures, for all possible combinations of semiconducting TMDC monolayers: MoS_2 , MoSe_2 , WS_2 , and WSe_2 . n -type WS_2 with WSe_2 triangular inclusions is found to have $ZT \approx 1$ at room temperature, which is five times larger than the ZT value of pristine n -type 1L WS_2 . The peak room-temperature power factors calculated for lateral TMDC heterostructures here are the highest amongst gapped 2D monolayers reported to date.

I. RESULTS

A. Nature of scattering in TMDC heterostructures

We calculated thermoelectric properties using the Boltzmann transport theory under the relaxation time approximations. Within this framework, the kinetic definitions of the conductance, Seebeck coefficient, and the electrical thermal conductivity are given by

$$\begin{aligned} \sigma &= e^2 \mathcal{I}_0, \\ S &= \frac{1}{eT} \frac{\mathcal{I}_1}{\mathcal{I}_0}, \\ \kappa_e &= \frac{1}{T} \left[\mathcal{I}_2 - \frac{\mathcal{I}_1^2}{\mathcal{I}_0} \right], \end{aligned} \quad (2)$$

with

$$\mathcal{I}_n = \int dE v^2 \tau(E) g(E) (E - \mu_F)^n \left(-\frac{\partial f_0}{\partial E} \right), \quad (3)$$

where e is the elementary charge, $g(E)$ is the density of states, $v = |\nabla_k E_n(k)|/\hbar$ is the carrier velocity,

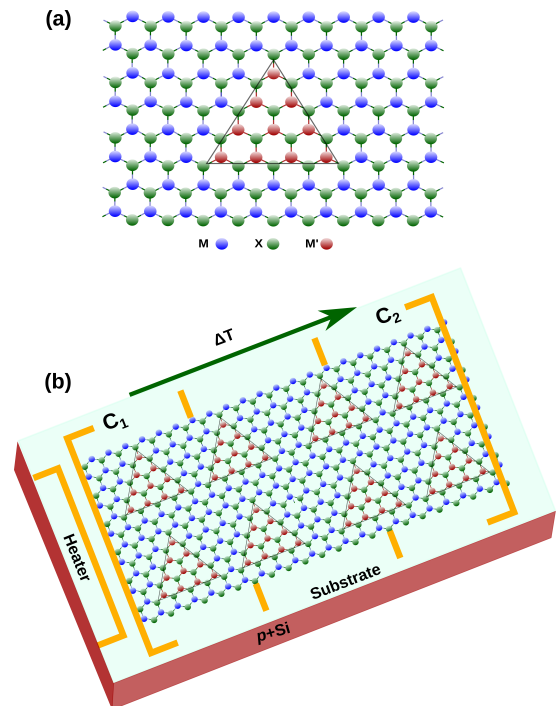


FIG. 1. A schematic representation of (a) a triangular inclusion in 2D materials is displayed. Here, $M'X_2$ material is confined within the MX_2 matrix. (b) An in-plane thermoelectric device using lateral TMDC heterostructures is shown. The 2D monolayer is placed on an oxide substrate that can be grown on p -silicon material.

$f_0(E) = 1/(1 + e^{(E - \mu_F)/k_B T})$ is the Fermi-Dirac distribution function, μ_F is the Fermi level, and $\tau(E)$ is the total scattering time. The density of states $g(E)$ is extracted from the electronic band structure obtained using the density functional theory (DFT) calculations within the local-density approximations (LDA). Figure 2 displays the density of states as a function of energy for 1L MoS_2 , WS_2 , MoSe_2 and WSe_2 . Here, $g(E)$ is normalized by the unit-cell area and the corresponding layer thickness. The PF and ZT values are sensitive to the small variations of $g(E)$ near the band edges.

To determine $\tau(E)$, we need to consider both the intrinsic and extrinsic scattering rates. According to the Matthiessen's law

$$\tau(E)^{-1} = \tau_e(E)^{-1} + \tau_{ph}(E)^{-1}, \quad (4)$$

where τ_e is the extrinsic carrier scattering time arising from the material inclusions, and τ_{ph} is the total intrinsic scattering time arising from all the acoustic and optical phonon mode contributions. The intrinsic scattering rate τ_{ph} is assumed to remain unaltered from the pristine 1L, a commonly used assumption while studying nanostructured thermoelectric materials [46].

Figure 3 shows the total phonon scattering time versus energy at room temperature for pristine n -type and p -type 1L TMDCs. We have included the acoustic and

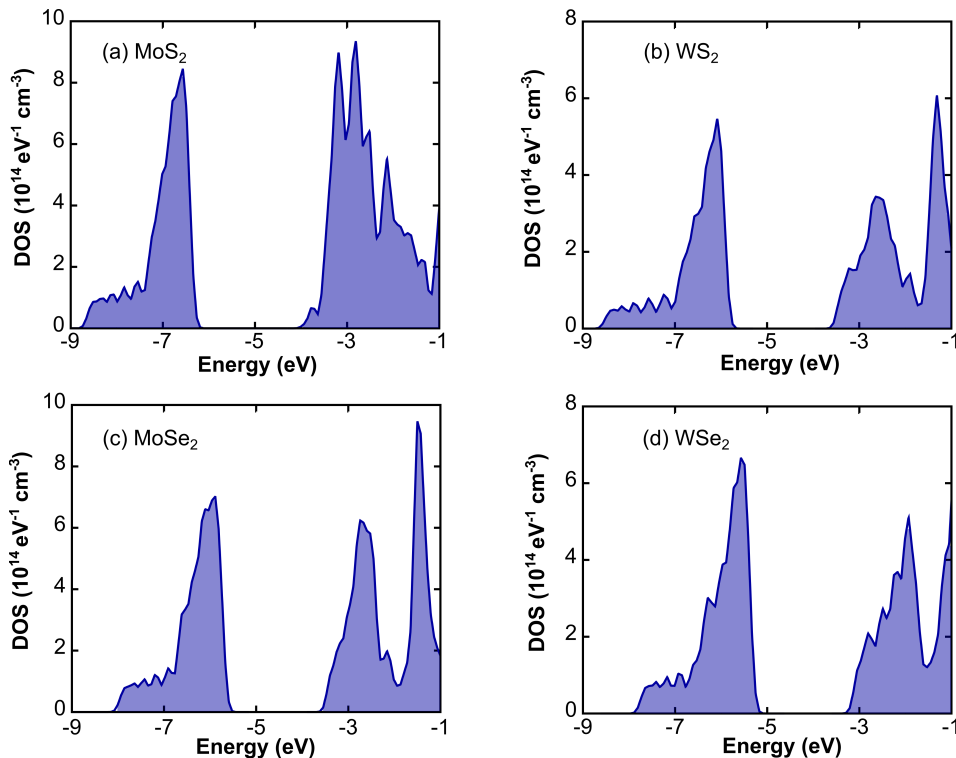


FIG. 2. Density of states per unit energy per unit area obtained from DFT calculations is plotted as a function of energy for 1L (a) MoS₂, (b) WS₂, (c) MoSe₂, and (d) WSe₂. DFT calculations were performed within local-density approximations (LDA), and the spin-orbit effects are neglected. Hence, all bands are doubly degenerate. The zero of the energy scale is at the vacuum. Bandgaps observed here were corrected to match the GW calculations.

optical phonon modes corresponding to the transitions, $K \rightarrow \{K, K', Q, Q'\}$, via corresponding zeroth and first-order deformation potentials (see Methods for details). The optical phonon modes emerge as steps in the scattering rate. In the family of 1L TMDCs, MoSe₂ (WS₂) has the strongest (weakest) interaction with phonons. In general, WX₂ has a greater phonon-limited electrical conductivity than MoX₂. These observations and scattering times are consistent with other first-principles studies reported in the literature [40, 41].

To calculate the carrier scattering time τ_e , we have employed a multiscale quantum transport framework informed by first-principles calculations described in Ref. [47]. Material inclusions break the translation symmetry of the system. Hence, scattering in these heterostructures can occur via both propagating (real wavevector) and evanescent modes (purely imaginary wavevector). As an example, in Fig. 4, we have plotted the heterointerface formed between 1L MoS₂ and WS₂. Electronic structure calculations dictate that 1L MoS₂ ($E_c = -4.31$ eV) has a lower conduction band (CB) minimum than 1L WS₂ ($E_c = -3.97$ eV). When an electron in the CB with energy $-4.31 \text{ eV} \leq E < -3.97$ eV is injected from 1L MoS₂ to WS₂, scattering occurs only through the evanescent modes. Similarly, for carriers in the valence band of p -type WS₂, with energy $-5.50 \text{ eV} \geq E > -5.89$ eV (corresponding to the valence

band maximum of MoS₂) only evanescent modes are available for scattering. Evanescent modes are situated within the bandgap, and result in exponentially decaying contributions to the scattered wavefunction.

Thermoelectric quantities in Eq. (2) are directly proportional to the total scattering time $\tau(E)$. Figure 5 displays the electron scattering rate, $1/\tau_e$, as a function of energy for four different n -type material combinations. We see that WS₂(MoS₂) has a higher scattering time (inverse of the scattering rate) while compared to MoS₂(WS₂). A similar trend is followed by WSe₂(MoSe₂) and MoSe₂(WSe₂) 1L as well.

B. Power factor and ZT values in TMDC heterostructures

The main results for the peak power factor and ZT values for the n -type and p -type TMDC lateral heterostructures are listed in Table I and Table II, respectively. In these tables, the notation A(B) represents that the material B inclusions are confined within the matrix of the material A. The material inclusion is considered here to be an equilateral triangle.

We observe that the n -type WS₂(WSe₂), and p -type

TABLE I. The peak power factor (PF) and the figure-of-merit ZT are listed for n -type monolayer (1L) TMDC heterostructures at temperatures 300 K, 500 K, and 800 K. Here, the notation A(B) represents that the material B inclusions are confined within the matrix of the material A. The material inclusion is equilateral triangle of the side length 8 nm. The density of inclusions is considered to be, $n_d = 10^{12} \text{ cm}^{-2}$. For comparison, we have listed the room temperature ZT values for pristine 1L TMDCs obtained via our scattering calculations along with values reported in the literature Refs. [21, 22].

1L heterostructure	PF ($10^{-3} \text{ WK}^{-2} \text{ m}^{-1}$)			ZT			Pristine 1L (at 300 K)				
	A (B)	300 K	500 K	800 K	300 K	500 K	800 K	A	ZT_{1L}	ZT_{1L} [21]	ZT_{1L} [22]
MoS ₂ (WS ₂)		0.365	0.293	0.181	0.093	0.124	0.125	MoS ₂	0.25	0.22	0.25
MoS ₂ (MoSe ₂)		0.335	0.256	0.167	0.084	0.109	0.115	MoS ₂	0.25	0.22	0.25
WS ₂ (MoS ₂)		4.565	3.896	2.371	0.598	1.231	1.641	WS ₂	0.20	0.22	0.23
WS ₂ (WSe ₂)		5.977	4.476	2.470	0.997	1.611	1.806	WS ₂	0.20	0.22	0.23
MoSe ₂ (WSe ₂)		0.500	0.367	0.200	0.173	0.227	0.205	MoSe ₂	0.38	0.35	0.36
MoSe ₂ (MoS ₂)		0.485	0.362	0.199	0.165	0.223	0.205	MoSe ₂	0.38	0.35	0.36
WSe ₂ (MoSe ₂)		1.929	1.457	0.815	0.485	0.816	0.875	WSe ₂	0.30	0.33	0.38
WSe ₂ (WS ₂)		1.954	1.468	0.819	0.488	0.821	0.879	WSe ₂	0.30	0.33	0.38

MoSe₂(WSe₂) have the maximum ZT values at room temperature. On the other hand, n -type WS₂(WSe₂), n -type WS₂(MoS₂), and p -type MoS₂(MoSe₂) have larger ZT values at higher temperatures. In Tables I and II, for comparison, we have listed the room temperature ZT values for pristine 1L TMDCs obtained from Refs. [21, 22]. For the n -type 1L WS₂ we observe up to five times larger ZT value with WSe₂ inclusions as compared to pristine n -type WS₂ 1L. Similarly, for p -type MoSe₂ with WSe₂ inclusions, we observe an enhancement by a factor of two in the ZT values as compared to pristine 1L MoSe₂. In general, ZT values increase with temperature, as there is a multiplicative factor of temperature in Eq. (1).

The calculated peak value of the PF for n -type 1L WS₂(WSe₂) and WS₂(MoS₂) at room temperature is $5.977 \text{ mWK}^{-2} \text{ m}^{-1}$ and $4.565 \text{ mWK}^{-2} \text{ m}^{-1}$, respectively. These values are about twice the peak PF value observed in the corresponding pristine 1L TMDCs [27]. Moreover, they are of the same order of magnitude as the observed PF in traditional thermoelectric materials, such as Bi₂Ti₃ ($5.2 \text{ mWK}^{-2} \text{ m}^{-1}$ [44]) and BiSbTe ($5.4 \text{ mWK}^{-2} \text{ m}^{-1}$ [45]) crystals.

In Table I, we observe that n -type MoS₂(WS₂) and MoS₂(MoSe₂) have significantly lower thermoelectric values compared to a pristine MoS₂ 1L. Similarly, p -type WSe₂(WS₂) and WSe₂(MoSe₂) have significantly lower thermoelectric values compared to a pristine WSe₂ 1L (see Table II). These phenomena can be explained as a direct consequence of band alignment as explained in the next section.

C. Band alignments and the thermoelectric enhancement

In Fig. 6, we observe that 1L WS₂ has a higher CB minimum at the K -valley than 1L MoS₂. Hence, MoS₂ inclusions provide additional conduction channels for electrons entering from the n -type 1L WS₂. This will increase the electron scattering time as seen in Fig. 5. On the other hand, in the n -type MoS₂ with WS₂ inclusions, scattering occurs through the evanescent modes offered by the WS₂ inclusion. This will significantly decrease the scattering time. Moreover, being real functions the evanescent modes indirectly decrease the probability current by draining the probability of propagating channels, thereby, significantly reducing the conductance values.

The total scattering time $\tau(E)$ follows the reciprocal sum rule defined in Eq. (4). Hence, the lower of the two scattering times between τ_{ph} and τ_e will be the dominating contributor to the thermoelectric quantities. For transport in n -type MoS₂(WS₂) 1L, τ_e is an order of magnitude lower than τ_{ph} around the band edge. Hence, we obtain low values of PF and ZT values as shown in Table I.

In p -type heterostructures, the valence band (VB) maxima between the two layers determine the occurrence of evanescent modes. In Fig. 6, we see that WS₂ has a higher VB maximum than MoS₂. Thus scattering in the p -type WS₂(MoS₂) occurs through evanescent modes. Hence, we observe that the p -type WS₂ heterostructures have lower ZT values while compared to the corresponding pristine monolayer as seen in Table II. Due to additional conduction channels offered by the WS₂ inclu-

TABLE II. The peak power factor (PF) and the figure-of-merit ZT are listed for p -type monolayer (1L) TMDC heterostructures at temperatures 300 K, 500 K, and 800 K. Here, the notation A(B) represents that the material B inclusions are confined within the matrix of the material A. The material inclusion is considered to be an equilateral triangle of the side length 8 nm. The density of inclusions is considered to be, $n_d = 10^{12} \text{ cm}^{-2}$. For comparison, we have listed the room temperature ZT values for pristine 1L TMDCs obtained via our scattering calculations along with values reported in the literature Refs. [21, 22].

1L heterostructure	PF ($10^{-3} \text{ WK}^{-2} \text{ m}^{-1}$)			ZT			Pristine 1L (at 300 K)				
	A (B)	300 K	500 K	800 K	300 K	500 K	800 K	A	ZT_{1L}	ZT_{1L} [21]	ZT_{1L} [22]
MoS ₂ (WS ₂)		1.940	1.862	1.315	0.407	0.713	0.871	MoS ₂	0.50	0.47	0.53
MoS ₂ (MoSe ₂)		4.076	3.213	2.001	0.648	1.115	1.289	MoS ₂	0.50	0.47	0.53
WS ₂ (MoS ₂)		0.895	0.779	0.568	0.274	0.407	0.486	WS ₂	0.40	0.43	0.42
WS ₂ (WSe ₂)		1.274	1.203	0.873	0.370	0.607	0.736	WS ₂	0.40	0.43	0.42
MoSe ₂ (WSe ₂)		2.272	1.826	1.060	0.714	1.004	1.045	MoSe ₂	0.42	0.38	0.39
MoSe ₂ (MoS ₂)		2.015	1.554	0.945	0.560	0.861	0.934	MoSe ₂	0.42	0.38	0.39
WSe ₂ (MoSe ₂)		0.034	0.023	0.014	0.015	0.017	0.016	WSe ₂	0.35	0.34	0.35
WSe ₂ (WS ₂)		0.023	0.017	0.011	0.011	0.013	0.013	WSe ₂	0.35	0.34	0.35

sions, an enhancement in the ZT and PF values are observed in the p -type 1L MoS₂(WS₂). An analogous mechanism explains the enhancement observed in p -type MoSe₂(WSe₂), which has the highest room temperature ZT value amongst the p -type heterostructures.

Figure 7 displays the conductance, Seebeck coefficient, PF, and electrical thermal conductivity as a function of the reduced Fermi-level $\eta_F = (E - E_c)/k_B T$ for n -type MoS₂(WS₂), and n -type WS₂(MoS₂) 1L heterostructures. Note that σ and κ_e monotonically increase with η_F . Comparing Fig. 7(a) and (e), we observe a significant enhancement in σ for WS₂(MoS₂) as reasoned earlier, whereas the Seebeck coefficient remains of the same order for both the heterostructures. Hence, we obtain high PF and ZT values for the n -type 1L WS₂(MoS₂) heterostructures. A similar trend is followed by other material combinations as well. We note that the PF increases slightly with increase in the width of material inclusions, and we found it to be optimized for the side length of 8 nm for the equilateral triangle inclusions. Unlike Schrödinger particles, the massive Dirac particles in TMDC inclusions have a critical length below which they will not occupy any bound states [48]. Thus, for inclusions with edges smaller than this critical length, heterostructures considered here will have the thermoelectric values similar to that of 1L pristine.

II. CONCLUSIONS

In this work, we investigated the thermoelectric properties of semiconducting transition metal dichalcogenide

lateral heterostructures using a multiscale quantum transport framework. We reported a new mechanism to enhance the thermoelectric efficiency in 2D materials by adding conduction channels through lateral heterostructures. The n -type WS₂ monolayer with WSe₂ inclusions has the highest room-temperature ZT values, which is about five times larger than the pristine WS₂ monolayer. The p -type MoSe₂ monolayer with WSe₂ inclusions is observed to have a room-temperature ZT value about two times larger than the pristine MoSe₂ monolayer. The peak PF values calculated in these heterostructures are of the same order of magnitude as traditional high-performance thermoelectric materials such as Bi₂Ti₃ and BiSbTe. The PF values reported here, are also the highest amongst gapped 2D monolayers. We expect the given mechanism to show similar enhancement of thermoelectric power in oxide and other monolayer heterostructures. Hence, 2D lateral heterostructures provide exciting new avenues to develop ultra-efficient in-plane thermoelectric devices.

III. METHODS

To determine the thermoelectric quantities in Eq. (2) we need to determine the density of states $g(E)$ and the total scattering time $\tau(E)$. The density of states $g(E)$ is computed from DFT calculations. The phonon and electron scattering contributions of $\tau(E)$ are determined independently.

DFT calculations were performed, using the Vienna Ab Initio Simulation Package (VASP) [49, 50], to obtain the

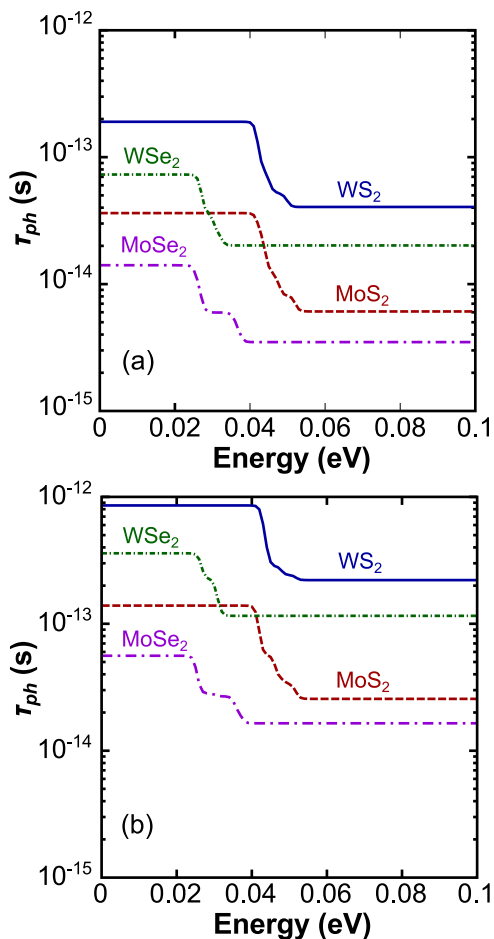


FIG. 3. The total phonon scattering time versus energy for (a) K -valley electrons, and (b) K -valley holes are plotted for TMDCs at temperature $T = 300$ K. Scattering times are calculated using the deformation potentials listed in Ref. [40–42].

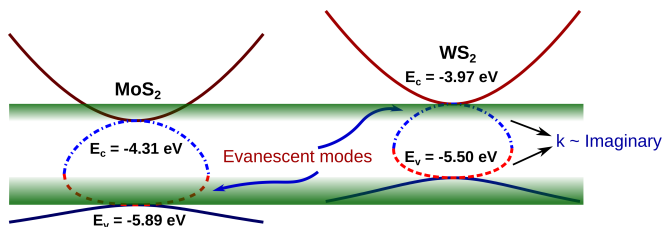


FIG. 4. The conduction and valence band near the K -point are plotted for MoS₂ and WS₂ 1L. In the presence of scattering centers, below the energy -3.97 eV (for n -type MoS₂), and above the energy -5.89 eV (for p -type WS₂) carrier transport across the interface occurs only through the evanescent bands.

density of states for the various TMDC monolayers studied here. Core and valence electrons were modeled using the projector-augmented wave (PAW) method [51, 52] and the local density approximation [53, 54] was used to describe electron exchange and correlation. The kinetic energy cutoff was set to 500 eV and a Gaussian smear-

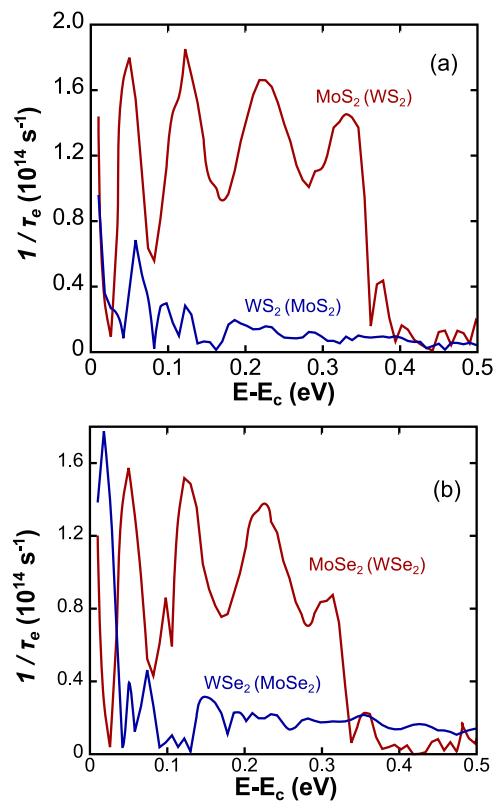


FIG. 5. The electron scattering rates versus energy for a K -valley electron are plotted for transport in (a) MoS₂(WS₂) & WS₂(MoS₂), and (b) MoSe₂(WSe₂) & WSe₂(MoSe₂) 1L heterostructures. For simplicity, we denote WS₂ monolayer with MoS₂ inclusions as WS₂(MoS₂). Same notation applies for all other combinations as well.

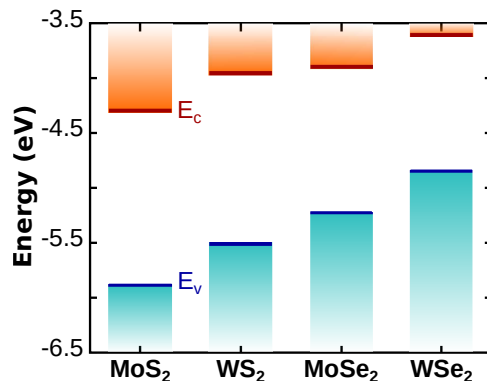


FIG. 6. The bar chart displays the band alignment in the semiconducting TMDC 1L. The conduction band minimum and the valence band maximum are represented by E_c and E_v , respectively. These numerical values are listed in Table III.

ing of 0.1 eV was used for Brillouin-zone integrations. The Brillouin zones were sampled using an $18 \times 18 \times 1$ Γ -centered k -point mesh. The lattice parameters for the TMDC monolayers were fixed at the bulk experimental parameters (MoS₂: [55]; MoSe₂: [56]; WS₂ & WSe₂: [57]). As semilocal functionals underestimate the fun-

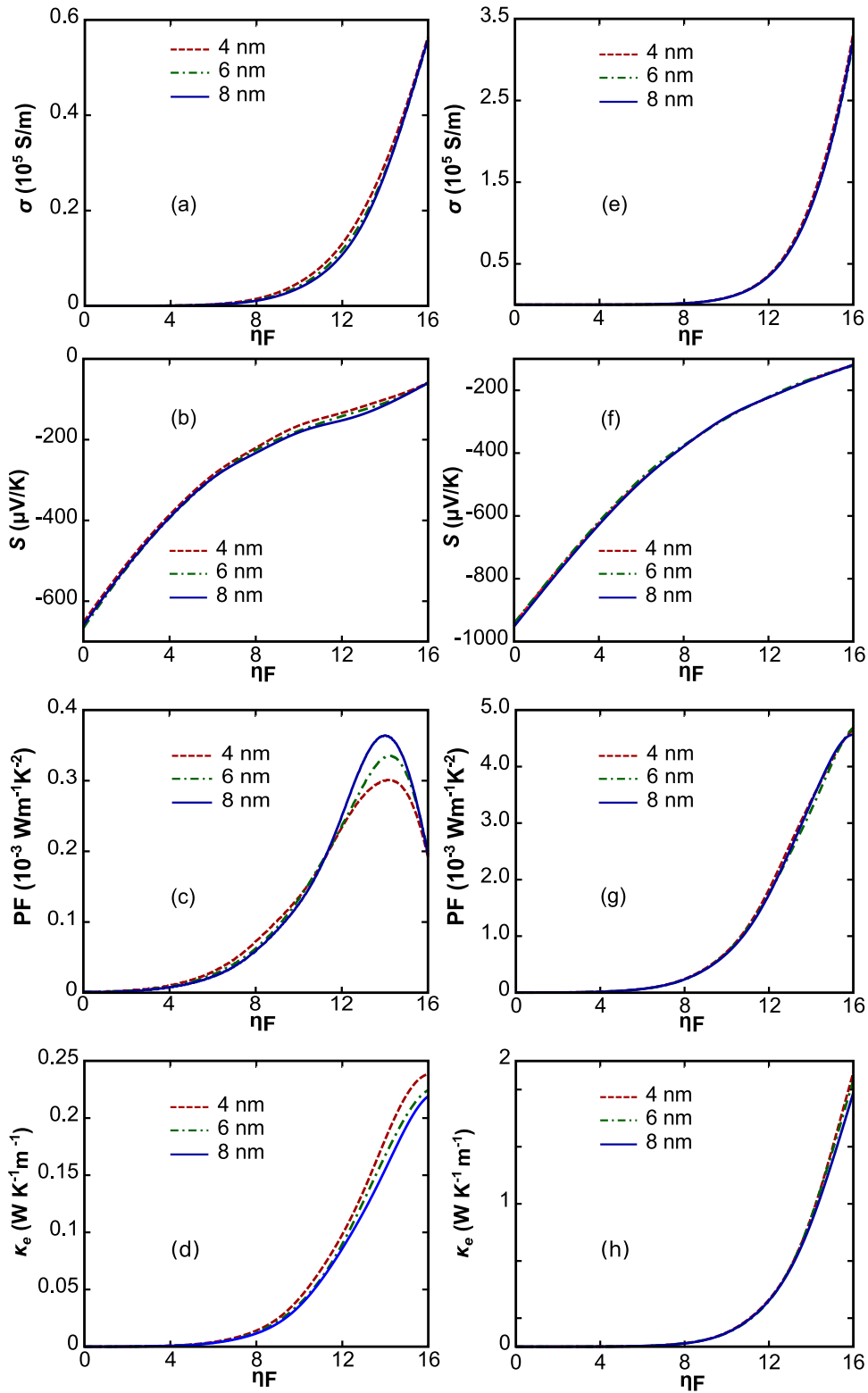


FIG. 7. The conductance, Seebeck coefficient, power factor, and electrical-thermal conductivity are plotted as a function of the reduced Fermi-level $\eta_F = (E - E_c)/k_B T$ for the n -type $\text{MoS}_2(\text{WS}_2)$, and n -type $\text{WS}_2(\text{MoS}_2)$ 1L heterostructures. We have considered triangular material inclusions of radius 4, 6, and 8 nm.

damental gaps of semiconductors, the density of states were shifted, *a posteriori*, to match the quasiparticle gaps

reported in Ref. [39].

The deformation potentials obtained from first-

principles calculations [40, 41] were employed to compute both the acoustic and optical phonon mode contributions. We have included the zeroth order acoustic and optical, and first order acoustic mode contributions. The effect of the Fröhlich interaction is implicitly added to the deformation potential [41]. The total τ_{ph} is determined using the reciprocal sum of these contributions as prescribed by Matthiessen’s law. Further details of these calculations can be found in Ref. [47].

For elastic scattering processes in 2D, the kinetic definition of τ_e is given by $\tau_e(E) = 1/(n_d \sigma_m \langle v \rangle)$, where n_d is the disorder density, $\langle v \rangle$ is the average velocity, and σ_m is the momentum scattering cross-section. $\langle v \rangle = 2v/\pi$ for a uniform incoming velocity distribution. σ_m is determined using a multiscale quantum transport framework [47]. Carrier scattering in lateral heterostructures occurs via both propagating and evanescent modes. Standard scattering calculations cannot account for these crucial contributions of decaying evanescent modes, since their probabilities vanish at the asymptotic limit, where the boundary conditions are applied to determine the scattering amplitudes. On the other hand, our methodology accurately includes these contributions since we have circumvented the need for the asymptotic boundary conditions by introducing absorbers around the scattering centers.

Scattering properties are determined through a 2-band

$\mathbf{k} \cdot \mathbf{p}$ Hamiltonian of the form

$$H_{kp} = H_0 + at (\eta k_x \hat{\sigma}_x + ik_y \hat{\sigma}_y) - \lambda \eta \frac{(\hat{\sigma}_z - 1)}{2} s, \quad (5)$$

where $\hat{\sigma}$ denotes the Pauli matrices, a is the lattice constant, t is the effective hopping integral, λ is the spin-orbit (SO) parameter, and H_0 is given by

$$H_0 = \begin{bmatrix} E_c + \alpha_s k^2 & 0 \\ 0 & E_v \end{bmatrix}. \quad (6)$$

Here, α_s is a material parameter, and E_c and E_v are the CB minimum and the VB maximum at the K -valley, respectively. All the material parameters employed in this article are listed in Table III. A detailed discussion of the quantum transport framework employed here is described in Ref. [47]. The quantum transport calculations combined with the Boltzmann transport theory determine σ , S and κ_e (see Eq. (2)). To determine the ZT factor we also require the phonon thermal conductivity κ_{ph} (see Eq. (1)). Typically κ_{ph} is computed through the phonon dispersion relations. We have utilized the κ_{ph} values listed in Ref. [21], that are obtained using DFT calculations.

ACKNOWLEDGMENTS

Calculations presented here were performed using computational resources supported by the Academic and Research Computing Group at WPI.

-
- [1] M. S. Dresselhaus, G. Chen, M. Y. Tang, R. G. Yang, H. Lee, D. Z. Wang, Z. F. Ren, J. P. Fleurial, P. Gogna, *New Directions for Low-Dimensional Thermoelectric Materials*, Adv. Mater. **19**, 1043–1053 (2007).
- [2] G. Chen, M. S. Dresselhaus, G. Dresselhaus, J. P. Fleurial, and T. Caillat, *Recent developments in thermoelectric materials*, International Materials Reviews **48**, 45–66 (2003).
- [3] C. J. Vineis, A. Shakouri, A. Majumdar, and M. G. Kanatzidis, *Nanostructured Thermoelectrics: Big Efficiency Gains from Small Features*, Adv. Mater. **22**, 3970–3980 (2010).
- [4] R. Franz and G. Wiedemann, *Über die Wärme-Leitungsfähigkeit der Metalle*, Annalen der Physik **165**, 497–531 (1853).
- [5] D. M. Rowe, *Thermoelectrics Handbook: Macro to Nano*, (CRC Press, Boca Raton, Florida, 2005).
- [6] L. D. Hicks and M. S. Dresselhaus, *Thermoelectric figure of merit of a one-dimensional conductor*, Phys. Rev. B **47**, 16631–16634 (1993).
- [7] L. D. Hicks and M. S. Dresselhaus, *Effect of quantum-well structures on the thermoelectric figure of merit*, Phys. Rev. B **47**, 12727–12731 (1993).
- [8] L. D. Hicks, T. C. Harman, X. Sun and M. S. Dresselhaus, *Experimental study of the effect of quantum-well structures on the thermoelectric figure of merit*, Phys. Rev. B **53**, R10493–R10496 (1996).
- [9] N. T. Hung, E. H. Hasdeo, A. R. T. Nugraha, M. S. Dresselhaus and R. Saito, *Quantum Effects in the Thermoelectric Power Factor of Low-Dimensional Semiconductors*, Phys. Rev. Lett. **117**, 036602 (2016).
- [10] A. Majumdar, *Thermoelectricity in Semiconductor Nanostructures*, Science **303**, 777–778 (2004).
- [11] Y. Pei, H. Wang and G.J. Snyder, *Band Engineering of Thermoelectric Materials*, Adv. Mater. **24**, 6125–6135 (2012).
- [12] T. Koga, X. Sun, S. B. Cronin, and M. S. Dresselhaus, *Carrier pocket engineering to design superior thermoelectric materials using GaAs/AlAs superlattices*, Appl. Phys. Lett. **73**, 2950–2952 (1998).
- [13] J.-H. Bahk, Z. Bian, and A. Shakouri, *Electron energy filtering by a nonplanar potential to enhance the thermoelectric power factor in bulk materials*, Phys. Rev. B **87**, 075204 (2013).
- [14] Y.-M. Lin, O. Rabin, S. B. Cronin, J. Y. Ying, and M. S. Dresselhaus, *Semimetal–semiconductor transition in $Bi_{(1-x)}Sb_x$ alloy nanowires and their thermoelectric properties*, Appl. Phys. Lett. **81**, 2403–2405 (2002).
- [15] M. Zebarjadi, *An Overview of 2D Materials for Thermoelectric Applications*, Celebrating Millie (2018). Available

	E_c	E_v	a	t	λ	$\alpha_+(\alpha_-)$	m_K^c	m_K^v
	(eV)	(eV)	(Å)	(eV)	(eV)	$\text{eV}\cdot\text{Å}^2$	(m_e)	(m_e)
MoS ₂	-4.31	-5.89	3.184	1.059	0.073	-5.97(-6.43)	0.45	0.53
WS ₂	-5.97	-5.50	3.186	1.075	0.211	-6.14(-7.95)	0.3	0.34
MoSe ₂	-3.91	-5.23	3.283	0.940	0.090	-5.34(-5.71)	0.53	0.58
WSe ₂	-3.61	-4.85	3.297	1.190	0.230	-5.25(-6.93)	0.33	0.36

TABLE III. The band parameters used in our calculations are listed. These parameters were obtained from the previously reported first-principles study [39, 43].

- from: <https://millie.pubpub.org/pub/b0fn884z>
- [16] F. Bonaccorso, L. Colombo, G. Yu, M. Stoller, V. Tozzini, A. C. Ferrari, R. S. Ruoff, and V. Pellegrini, *Graphene, related two-dimensional crystals, and hybrid systems for energy conversion and storage*, *Science* **347**, 1246501 (2015).
- [17] J. Duan, X. Wang, X. Lai, G. Li, K. Watanabe, T. Taniguchi, M. Zebbarjadi, and E. Y. Andrei, *High thermoelectric power factor in graphene/hBN devices*, *Proc. Natl Acad. Sci.* **113**, 14272–14276 (2016).
- [18] S. Chen, A.L. Moore, W. Cai, J.W. Suk, J. An, C. Mishra, C. Amos, C.W. Magnuson, J. Kang, L. Shi, and R.S. Ruoff, *Raman Measurements of Thermal Transport in Suspended Monolayer Graphene of Variable Sizes in Vacuum and Gaseous Environments*, *ACS Nano* **5**, 321 (2010).
- [19] S. Chen, Q. Wu, C. Mishra, J. Kang, H. Zhang, K. Cho, W. Cai, A.A. Balandin, R.S. Ruoff, *Thermal conductivity of isotopically modified graphene*, *Nat Mater* **11**, 203 (2012).
- [20] Y. Cai, J. Lan, G. Zhang, and Y.-W. Zhang, *Lattice vibrational modes and phonon thermal conductivity of monolayer MoS₂*, *Phys. Rev. B* **89**, 035438 (2014).
- [21] G. Ozbal, R. T. Senger, C. Sevik, and H. Sevincli, *Ballistic thermoelectric properties of monolayer semiconducting transition metal dichalcogenides and oxides*, *Phys. Rev. B* **100**, 085415 (2019).
- [22] W. Huang, H. Da, and G. Liang, *Thermoelectric performance of MX₂ (M: Mo, W; X: S, Se) monolayers*, *J. Appl. Phys.* **113**, 104304 (2013).
- [23] W. Huang, X. Luo, C. K. Gan, S. Y. Quek, and G. Liang, *Theoretical study of thermoelectric properties of few-layer MoS₂ and WSe₂*, *Phys. Chem. Chem. Phys.* **16**, 10866 (2014).
- [24] D. Wickramaratne, F. Zahid, and R. K. Lake, *Electronic and thermoelectric properties of few-layer transition metal dichalcogenides*, *J. Chem. Phys.* **140**, 124710 (2014).
- [25] H. Babaei, J. M. Khodadadi, and S. Sinha, *Large theoretical thermoelectric power factor of suspended single-layer MoS₂*, *Appl. Phys. Lett.* **105**, 193901 (2014).
- [26] B. Ouyang, S. Chen, Y. Jing, T. Wei, S. Xiong, and D. Donadio, *Enhanced thermoelectric performance of two dimensional MS₂ (M = Mo, W) through phase engineering*, *J. Materiomics* **4**, 329–337 (2018).
- [27] K. Hippalgaonkar, Y. Wang, Y. Ye, D. Y. Qiu, H. Zhu, Y. Wang, J. Moore, S. G. Louie, and X. Zhang, *High thermoelectric power factor in two-dimensional crystals of MoS₂*, *Phys. Rev. B* **95**, 115407 (2017).
- [28] T. Zhu, K. Swaminathan-Gopalan, K. Stephani, and E. Ertekin, *Thermoelectric phonon-glass electron-crystal via ion beam patterning of silicon*, *Phys. Rev. B* **97**, 174201 (2018).
- [29] M. Kayyalha, J. Maassen, M. Lundstrom, L. Shi, and Y. P. Chen, *Gate-tunable and thickness-dependent electronic and thermoelectric transport in few-layer MoS₂*, *J. Appl. Phys.* **120**, 134305 (2016).
- [30] X. Duan, C. Wang, J. C. Shaw, R. Cheng, Y. Chen, H. Li, X. Wu, Y. Tang, Q. Zhang, A. Pan, J. Jiang, R. Yu, Y. Huang, and X. Duan, *Lateral epitaxial growth of two-dimensional layered semiconductor heterojunctions*, *Nat. Nanotechnol.* **9**, 1024 (2014).
- [31] X.-Q. Zhang, C.-H. Lin, Y.-W. Tseng, K.-H. Huang, and Y.-H. Lee, *Synthesis of Lateral Heterostructures of Semiconducting Atomic Layers*, *Nano Lett.* **15**, 410 (2015).
- [32] M.-Y. Li, Y. Shi, C.-C. Cheng, L.-S. Lu, Y.-C. Lin, H.-L. Tang, M.-L. Tsai, C.-W. Chu, K.-H. Wei, J.-H. He, W.-H. Chang, K. Suenaga, and L.-J. Li, *Epitaxial growth of a monolayer WSe₂-MoS₂ lateral p-n junction with an atomically sharp interface*, *Science* **349**, 524 (2015).
- [33] C. Zhang, Y. Chen, J.-K. Huang, X. Wu, L.-J. Li, W. Yao, J. Tersoff, and C.-K. Shih, *Visualizing band offsets and edge states in bilayer-monolayer transition metal dichalcogenides lateral heterojunction*, *Nat. Commun.* **7**, 10349 (2016).
- [34] C. Zhang, M.-Y. Li, J. Tersoff, Y. Han, Y. Su, L.-J. Li, D. A. Muller, and C.-K. Shih, *Strain distributions and their influence on electronic structures of WSe₂-MoS₂ laterally strained heterojunctions*, *Nat. Nanotechnol.* **13**, 152 (2018).
- [35] P. K. Sahoo, S. Memaran, Y. Xin, L. Balicas, and H. R. Gutiérrez, *One-pot growth of two-dimensional lateral heterostructures via sequential edge-epitaxy*, *Nature* **553**, 63 (2018).
- [36] S. Xie, L. Tu, Y. Han, L. Huang, K. Kang, K. U. Lao, P. Poddar, C. Park, D. A. Muller, R. A. DiStasio, and J. Park, *Coherent, atomically thin transition-metal dichalcogenide superlattices with engineered strain*, *Science* **359**, 1131 (2018).
- [37] Y. Zhang, and G. D. Stucky, *Heterostructured Approaches to Efficient Thermoelectric Materials*, *Chem. Mater.* **26**, 837–848 (2014).
- [38] R. Venkatasubramanian, E. Siivola, T. Colpitts, and B. O’Quinn, *Thin-film thermoelectric devices with high room-temperature figures of merit*, *Nature* **413**, 597 (2001).

- [39] S. Hastrup, M. Strange, M. Pandey, T. Deilmann, P. S. Schmidt, N. F. Hinsche, M. N. Gjerding, D. Torelli, P. M. Larsen, A. C. Riis-Jensen, J. Gath, K. W. Jacobsen, J. J. Mortensen, T. Olsen, K. S. Thygesen, *The Computational 2D Materials Database: High-Throughput Modeling and Discovery of Atomically Thin Crystals*, *2D Materials* **5**, 042002 (2018).
- [40] K. Kaasbjerg, K. S. Thygesen, and K. W. Jacobsen, *Phonon-limited mobility in n-type single-layer MoS₂ from first principles*, *Phys. Rev. B* **85**, 115317 (2012).
- [41] Z. Jin, X. Li, J. T. Mullen, and K. W. Kim, *Intrinsic transport properties of electrons and holes in monolayer transition-metal dichalcogenides*, *Phys. Rev. B* **90**, 045422 (2014).
- [42] X. Li, J. T. Mullen, Z. Jin, K. M. Borysenko, M. B. Nardelli, and K. W. Kim, *Intrinsic electrical transport properties of monolayer silicene and MoS₂ from first principles*, *Phys. Rev. B* **87**, 115418 (2013).
- [43] A. Kormányos, G. Burkard, M. Gmitra, J. Fabian, V. Zólyomi, N. D. Drummond, and V. I. Fal'ko, *k-p theory for two-dimensional transition metal dichalcogenide semiconductors*, *2D Mater.* **2**, 022001 (2015).
- [44] C. Satterwaithe and R. Ure JR., *Electrical and Thermal Properties of Bi₂Te₃* *Phys. Rev.* **108**, 1164–1170 (1957).
- [45] T. Caillat, M. Carle, P. Pierrat, H. Scherrer, and S. Scherrer, *Thermoelectric properties of (Bi_xSb_{1-x})₂Te₃ single crystal solid solutions grown by the T.H.M. method*, *J. Phys. Chem. Solids* **53**, 1121 (1992).
- [46] J.-H. Lee, G. A. Galli, and J. C. Grossman, *Nanoporous Si as an Efficient Thermoelectric Material*, *Nano Lett.* **8**, 3750 (2008).
- [47] Sathwik Bharadwaj, Ashwin Ramasubramaniam, and L. R. Ram-Mohan (Submitted for publication).
- [48] C. C. Price, N. C. Frey, D. Jariwala, and V. B. Shenoy, *Engineering Zero-Dimensional Quantum Confinement in Transition-Metal Dichalcogenide Heterostructures*, *ACS Nano* **13**, 8303–8311 (2019).
- [49] G. Kresse, J. Furthmüller, *Efficiency of Ab-Initio Total Energy Calculations for Metals and Semiconductors Using a Plane-Wave Basis Set*, *Comput. Mater. Sci.* **6**, 15–50 (1996).
- [50] G. Kresse, J. Furthmüller, *Efficient Iterative Schemes for Ab Initio Total-Energy Calculations Using a Plane-Wave Basis Set* *Phys. Rev. B* **54**, 11169–11186 (1996).
- [51] P. E. Blöchl, *Projector Augmented-Wave Method* *Phys. Rev. B* **50**, 17953–17979 (1994).
- [52] G. Kresse, D. Joubert, *From Ultrasoft Pseudopotentials to the Projector Augmented-Wave Method* *Phys. Rev. B* **59**, 1758–1775 (1999).
- [53] D. M. Ceperley and B. J. Alder, *Ground State of the Electron Gas by a Stochastic Method*, *Phys. Rev. Lett.* **45**, 566 (1980).
- [54] J. P. Perdew and A. Zunger, *Self-interaction correction to density-functional approximations for many-electron systems*, *Phys. Rev. B* **23**, 5048 (1981).
- [55] B. Schönfeld, J. J. Huang, and S. C. Moss, *Anisotropic mean-square displacements (MSD) in single-crystals of 2H- and 3R-MoS₂* *Acta Cryst.* **B39**, 404–407 (1983).
- [56] P. B. James and M. T. Lavik, *The crystal structure of MoSe₂*, *Acta Cryst.* **16**, 1183 (1963).
- [57] W. J. Schutte, J. L. De Boer, F. Jellinek, *Crystal structures of tungsten disulfide and diselenide*, *J. Solid State Chem.* **70**, 207–209 (1987).